Science Advances
AAAS

advances.sciencemag.org/cgi/content/full/7/16/eabf4838/DC1

Supplementary Materials for

Optimal and continuous multilattice embedding

E. D. Sanders, A. Pereira, G. H. Paulino*

*Corresponding author. Email: paulino@gatech.edu

Published 16 April 2021, *Sci. Adv.* **7**, eabf4838 (2021)
DOI: 10.1126/sciadv.abf4838

The PDF file includes:

Supplementary Text
Figs. S1 to S9
Table S1
Legends for movies S1 to S3

Other Supplementary Material for this manuscript includes the following:

(available at advances.sciencemag.org/cgi/content/full/7/16/eabf4838/DC1)

Movies S1 to S3

S1 Constructing directional tensile and shear moduli plots

Hooke's Law is stated as $\sigma_{ij} = C_{ijk\ell}\varepsilon_{k\ell}$ or $\varepsilon_{ij} = Z_{ijk\ell}\sigma_{k\ell}$, $i, j, k, \ell = 1, 2, 3$, with Cauchy stress, σ_{ij}, linearized strain, $\varepsilon_{k\ell}$, homogenized stiffness elasticity tensor, $C_{ijk\ell}$, and homogenized compliance elasticity tensor, $Z_{ijk\ell} = C^{-1}_{ijk\ell}$. To gain insight about the stiffness of our microstructural-materials, we define two mechanical constants as follows: 1) the tensile modulus is obtained by imposing $\sigma_{11} \neq 0, \sigma_{ij} = 0, \forall ij \neq 11$ and using Hooke's Law to compute $E_{11} = \sigma_{11}/\varepsilon_{11} = 1/Z_{1111}$; and 2) the shear modulus is obtained by imposing $\sigma_{12} \neq 0, \sigma_{ij} = 0, \forall ij \neq 12, ji \neq 21$ and using Hooke's Law to compute $G_{12} = \sigma_{12}/(2\varepsilon_{12}) = 1/(2Z_{1212})$. These mechanical constants indicate the tensile stiffness of the microstructural-material in the x_1 direction and the shear stiffness of the microstructural-material in the $x_1 - x_2$ plane, respectively, with respect to a given reference (unprime) frame.

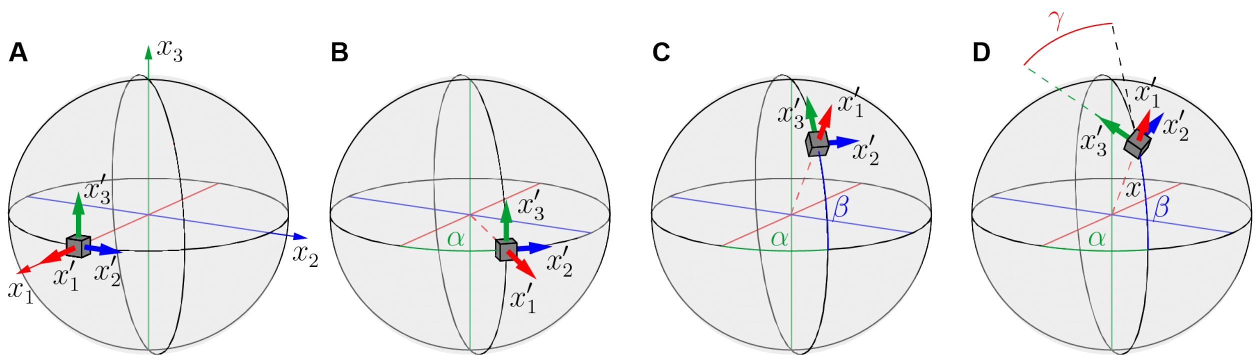

Fig. S1. Frame rotation conventions. (**A**) Rotated (prime) frame initially aligned with reference (unprime) frame. (**B**) Rotation about the x'_3 axis by α. (**C**) Rotation about the x'_2 axis by β. (**D**) Rotation about the x'_1 axis by γ.

To understand how these constants vary for different loading directions, we use tensor transformation laws to obtain the compliance elasticity tensor, $Z'_{ijk\ell}$, in a rotated (prime) frame. Let A_{ij} be a direction cosine matrix that transforms vectors from the reference to the rotated frame via a general rotation, i.e., $x'_i = A_{ij}x_j$. To construct A_{ij}, consider that the rotated frame is originally oriented with the reference frame (Fig. S1A), and orient it by first rotating about the x'_3 axis by α, then about the x'_2 axis by β, and finally about the x'_1 axis by γ as illustrated in Fig. S1B-D. These rotations can be expressed in terms of proper orthogonal matrices as follows:

$$R_1(\gamma) = \begin{bmatrix} 1 & 0 & 0 \\ 0 & c_\gamma & -s_\gamma \\ 0 & s_\gamma & c_\gamma \end{bmatrix}, \; R_2(\beta) = \begin{bmatrix} c_\beta & 0 & s_\beta \\ 0 & 1 & 0 \\ -s_\beta & 0 & c_\beta \end{bmatrix}, \; R_3(\alpha) = \begin{bmatrix} c_\alpha & -s_\alpha & 0 \\ s_\alpha & c_\alpha & 0 \\ 0 & 0 & 1 \end{bmatrix} \tag{1}$$

where $s_{(\cdot)}$ and $c_{(\cdot)}$ denote the sine and cosine of angle $(\cdot)$, respectively.

Let x be the position vector of the x'_1 axis in the reference frame after rotating (see Fig. S1D). Then the coordinate transformation can be expressed as $x = R_3(\alpha)\, R_2^T(\beta)\, R_1(\gamma)\, x'_1$, where we consider the transpose of $R_2(\beta)$ since β is defined as a negative rotation (see Fig. S1C). We invert this coordinate transformation to find that:

$$A_{ij} = R_1^T(\gamma)\, R_2(\beta)\, R_3^T(\alpha) = \begin{bmatrix} c_\beta c_\alpha & c_\beta s_\alpha & s_\beta \\ -s_\gamma s_\beta c_\alpha - c_\gamma s_\alpha & -s_\alpha s_\gamma s_\beta + c_\gamma c_\alpha & s_\gamma c_\beta \\ -c_\alpha c_\gamma s_\beta + s_\alpha s_\gamma & -s_\alpha c_\gamma s_\beta - s_\gamma c_\alpha & c_\gamma c_\beta \end{bmatrix} \tag{2}$$

Recall that if vectors transform as $x'_i = A_{ij}x_j$, then we know that second and fourth-order tensors transform as $\varepsilon'_{ij} = A_{ik}A_{j\ell}\varepsilon_{k\ell}$ and $Z'_{ijk\ell} = A_{im}A_{jn}A_{ko}A_{\ell p}Z_{mnop}$, respectively (similar expressions hold for transforming stress, σ_{ij}, and the stiffness elasticity tensor, $C_{ijk\ell}$). For convenience of computation, we convert to matrix (Voigt) notation by defining:

$$\{\sigma\} = \begin{Bmatrix} \sigma_1 = \sigma_{11} \\ \sigma_2 = \sigma_{22} \\ \sigma_3 = \sigma_{33} \\ \sigma_4 = \sigma_{23} \\ \sigma_5 = \sigma_{31} \\ \sigma_6 = \sigma_{12} \end{Bmatrix}, \{\varepsilon\} = \begin{Bmatrix} \varepsilon_1 = \varepsilon_{11} \\ \varepsilon_2 = \varepsilon_{22} \\ \varepsilon_3 = \varepsilon_{33} \\ \varepsilon_4 = 2\varepsilon_{23} \\ \varepsilon_5 = 2\varepsilon_{31} \\ \varepsilon_6 = 2\varepsilon_{12} \end{Bmatrix}, [D] = \left[\begin{array}{c|c} C_{ppqq} & C_{pprs} \\ \hline C_{pprs} & C_{pqrs} \end{array}\right], \text{ and } [S] = \left[\begin{array}{c|c} Z_{ppqq} & 2Z_{pprs} \\ \hline 2Z_{pprs} & 4Z_{pqrs} \end{array}\right] \quad (3)$$

From the stress and strain transformation laws in tensor notation, we can construct matrices, $[M]$ and $[N]$ that perform the transformations in matrix notation, where:

$$[M] = \left[\begin{array}{ccc|ccc} A_{11}^2 & A_{12}^2 & A_{13}^2 & 2A_{12}A_{13} & 2A_{13}A_{11} & 2A_{11}A_{12} \\ A_{21}^2 & A_{22}^2 & A_{23}^2 & 2A_{22}A_{23} & 2A_{23}A_{21} & 2A_{21}A_{22} \\ A_{31}^2 & A_{32}^2 & A_{33}^2 & 2A_{32}A_{33} & 2A_{33}A_{31} & 2A_{31}A_{32} \\ \hline A_{21}A_{31} & A_{22}A_{32} & A_{23}A_{33} & A_{22}A_{33}+A_{23}A_{32} & A_{21}A_{33}+A_{23}A_{31} & A_{22}A_{31}+A_{21}A_{32} \\ A_{31}A_{11} & A_{32}A_{12} & A_{33}A_{13} & A_{12}A_{33}+A_{13}A_{32} & A_{13}A_{31}+A_{11}A_{33} & A_{11}A_{32}+A_{12}A_{31} \\ A_{11}A_{21} & A_{12}A_{22} & A_{13}A_{23} & A_{12}A_{23}+A_{13}A_{22} & A_{13}A_{21}+A_{11}A_{23} & A_{11}A_{22}+A_{12}A_{21} \end{array}\right] \quad (4)$$

and

$$[N] = \left[\begin{array}{ccc|ccc} A_{11}^2 & A_{12}^2 & A_{13}^2 & A_{12}A_{13} & A_{13}A_{11} & A_{11}A_{12} \\ A_{21}^2 & A_{22}^2 & A_{23}^2 & A_{22}A_{23} & A_{23}A_{21} & A_{21}A_{22} \\ A_{31}^2 & A_{32}^2 & A_{33}^2 & A_{32}A_{33} & A_{33}A_{31} & A_{31}A_{32} \\ \hline 2A_{21}A_{31} & 2A_{22}A_{32} & 2A_{23}A_{33} & A_{22}A_{33}+A_{23}A_{32} & A_{21}A_{33}+A_{23}A_{31} & A_{22}A_{31}+A_{21}A_{32} \\ 2A_{31}A_{11} & 2A_{32}A_{12} & 2A_{33}A_{13} & A_{12}A_{33}+A_{13}A_{32} & A_{13}A_{31}+A_{11}A_{33} & A_{11}A_{32}+A_{12}A_{31} \\ 2A_{11}A_{21} & 2A_{12}A_{22} & 2A_{13}A_{23} & A_{12}A_{23}+A_{13}A_{22} & A_{13}A_{21}+A_{11}A_{23} & A_{11}A_{22}+A_{12}A_{21} \end{array}\right] \quad (5)$$

Then, substituting Hooke's Law, $\{\varepsilon\} = [S]\{\sigma\}$, and the stress transformation law, $\{\sigma\} = [M]^{-1}\{\sigma\}'$, into the strain transformation law, $\{\varepsilon\}' = [N]\{\varepsilon\}$, we find that $[S]' = [N][S][M]^{-1} = [N][S][N]^T$, where the last expression comes from the fact that $A_{ij} = A_{ij}^T$ since it is a product of proper orthogonal matrices. Now we can compute the tensile and shear moduli, $E'_{11} = 1/S'_{11}$ and $G'_{12} = 1/S'_{66}$, for any arbitrary orientation of the rotated coordinate frame by $\alpha, \beta,$ and γ. The above derivations are taken from Auld, 1973 (*77*) and Turley and Sines, 1971 (*76*).

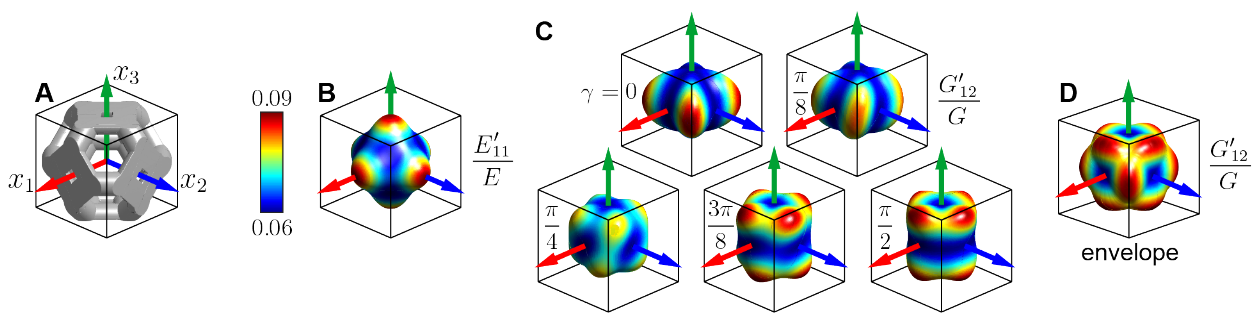

Fig. S2. Directional tensile and shear moduli plots. (**A**) Truncated octahedron unit cell geometry and corresponding (**B**) directional tensile moduli, (**C**) directional shear moduli for various γ rotations of the rotated frame, and (**D**) enveloped directional shear moduli for $\gamma = 0, \pi/16, \ldots, \pi$.

To visualize the directional tensile and shear moduli of a given microstructural-material, we generate a 3D surface plot where, for all possible rotations of the prime coordinate frame, a point is plotted along the x vector, which locates the rotated frame with respect to the reference frame, with radial coordinate equal to E'_{11} or G'_{12}. It is noted that there is only one way to represent the directional tensile modulus (with the x'_1 axis oriented in the radial direction of the reference frame), but there are infinite ways to represent the directional shear modulus depending on the orientation of the x'_2 and x'_3 axes about the x'_1 axis. An illustrative example is provided in Fig. S2 for a periodic material composed of a truncated octahedron unit cell. Unless otherwise noted, the shear modulus plots reported in the main text represent an envelope of critical orientations of shear ($\gamma = 0$ and $\gamma = \pi/2$ for the cubic materials considered here).

S2 Continuous multi-microstructure-embedding

The multi-material slicing and multi-microstructure-embedding scheme described in the main text is summarized in the flowchart in Fig. S3.

To complete the example shown in Fig. 1 and 3 of the main text, we show macro-slices, micro-slices, embedded-slices, and the macro-to-micro mapping used for the cantilever beam designed for two octahedron unit cells in Fig. S4A and for a face-x and center-x unit cell in Fig. S4B. Again, notice the smooth and continuous connectivity in the embedded-slices when considering the functionally graded structure.

Considering the two-microstructural-material beam composed of simple cubic and truncated octahedron unit cells (refer to Fig. 1B, 2B, and 3 of the main text), we generate the functionally-graded tet mesh using $R = 0$, 0.010, 0.025, 0.050, 0.100, and 0.200 to demonstrate how the length scale of the transition region, connectivity of the microstructures, and objective function value are affected by the filter radius, R, used in functional grading. To ensure that a sufficient number of tet elements are encompassed by the radius during filtering, we refine the tet mesh near the microstructural-material interfaces for the cases of $R \leq 0.050$. Note that $R = 0$ corresponds to the abrupt transition shown in Fig. 3C of the main text and $R = 0.100$ corresponds to the functionally-graded transition shown in Fig. 3D of the main text.

To achieve a well-connected interface between the microstructural-materials, the transition region must have a finite length. A rule of thumb is that the transition region should be at least as long as the edge length of the unit cells. In the printed part shown Fig. 1B, the edge length of the unit cells is 1.5 mm, which corresponds to an edgelength of 0.030 relative to the domain dimensions used during design and provided in Fig. 1 (the part was scaled up for manufacturing). When the filter radius is larger than 0.030 (i.e., $R = 0.050, 0.100, 0.200$), the microstructures are well-connected at the interfaces. When the filter radius is smaller than 0.030 (i.e., $R = 0.010, 0.0250$), we still achieve relatively good connectivity, but the interface may not be as robust. The objective function values, f, provided in Fig. S5 are normalized to that of the case with $R = 0$, which has objective function value, f_0. The normalized objective function values, f/f_0, indicate that the length scale of the transition regions does not significantly affect the global elastic properties of the structure.

S3 Effect of porous, anisotropic microstructural-materials in topology optimization

The normalized objective function values, f/f_0, in Fig. 4B-G of the main text, indicate how efficient each design is relative to the reference case in Fig. 4A (in terms of stiffness). The porous structures become more efficient as we increase the microstructural-material freedom (i.e., as the homogenized material properties of the available microstructural-materials become more diverse) because we are able to better represent the varying directions and magnitudes of the principal stresses. The beam in Fig. 4G, which has more microstructural-material freedom than the other multi-scale structures, is the most efficient, but still has much higher compliance than the solid, isotropic case because the design space is still limited by the available microstructural-materials. Moreover, using low volume fraction lattices as space filling structural elements forces material away from optimal regions and can lead to sub-optimal results. Although the solid, isotropic structure has superior stiffness, multi-scale structures tend to have increased buckling resistance (*47*) and can provide other biomimetic functionalities (e.g., buoyancy and impact resistance).

S4 Effect of initial guess and continuation scheme on the material interpolation parameters

The volume-constrained, compliance minimization problem in (1) is non-convex due to the material interpolation functions that penalize intermediate densities and material mixing. The initial guess and other algorithmic parameters play a role in the local optimum found; however, the continuation scheme on p and γ described in the "Materials and methods" section helps bias the solution toward that of the convex one at the beginning of the optimization iterations (i.e., by starting with $p = 1$ and $\gamma = 0$ to recover the convex problem).

To demonstrate the effectiveness of the continuation scheme in achieving a "good" local minimum, we re-run the 4-microstructural-material example from Fig. 4F considering four different initial guesses. In each case, one of the four candidate microstructural-materials dominates in the initial guess. Specifically, in each case, the initial densities of one of the microstructural-materials are specified at $0.85\overline{v}$ and the other three microstructural-materials' initial densities are specified at $0.05\overline{v}$. The results are provided in Fig. S6, where three of the four initial guesses (Fig. S6B-D) lead to results very similar to the one reported in the paper (repeated in Fig. S6A), which used a uniform initial guess. One of the four initial guesses arrives at a distinctly different local minimum (Fig. S6E) with different topology and a small region of microstructure 8 arising in the design. The objective function values of all four designs (normalized to that of the structure in Fig. 4A) are very similar. In general, we expect to obtain a local minimum, and the initial guess influences which local minimum we find; however, typically the local minima have similar elastic responses.

S5 Canopy and Eiffel tower-inspired structures

The candidate microstructural-materials, design domains, and boundary conditions for the canopy and Eiffel tower-inspired structures are provided in Fig. S7.

S6 Manufactured parts

In Table S1, we report the dimensions of a bounding box enclosing the computer model (after scaling for printing) and the m-SLA physical model for each design reported in the paper. In general, the overall dimensions of the manufactured parts are within 1 mm of the expected dimensions.

The support structures needed for printing the canopy structure, as designed in Rhino®, are shown in Fig. S8A. To save material, the support structures were embedded with octahedron unit cells with 2 mm edge length and 0.44 mm bar diameter. One half of the canopy structure before removing the support structure is shown on the build plate in Fig. S8B. The support structures were not fully attached the the canopy, making it relatively easy to remove them without damaging the delicate microstructures. In Fig. S8C, the canopy is shown before gluing the pieces together.

In Fig. S9, two cross-sections of the Eiffel Tower-inspired structure highlight some interesting macrostructural details: macroscale voids are present on the interior of the dome structure at floor 2 and the supports at the base branch several times to provide relatively uniform support at the first floor.

Table S1: Bounding box dimensions of computer and physical models for each design (cm)

	computer model	physical model
Cantilever (octahedron and octahedron)	$4.84 \times 4.96 \times 14.52$	$4.80 \times 5.05 \times 14.45$
Cantilever (simple cubic and truncated octahedron)	$4.84 \times 4.95 \times 14.52$	$4.80 \times 4.95 \times 14.45$
Cantilever (face-x and center-x)	$4.84 \times 5.07 \times 14.52$	$4.75 \times 5.05 \times 14.45$
Canopy	$11.72 \times 11.72 \times 14.65$	$11.60 \times 11.60 \times 14.40$
Eiffel tower	$8.09 \times 8.09 \times 26.30$	$8.10 \times 8.20 \times 25.95$

S7 Movie captions

Movie S1. Multiscale design and manufacturing. An animation of the design iterations, the post-processing needed to generate the transition regions, and the final manufactured part for the canopy structure.

Movie S2. Slicing and multi-microstructure-embedding. An animation of macro-slices, micro-slices, and embedded slices over the height of the canopy structure.

Movie S3. Microstructural-material property transitions. Animations showing how the unit cell geometries and associated material properties change over the transition regions for the two-microstructural-material cantilever beams.

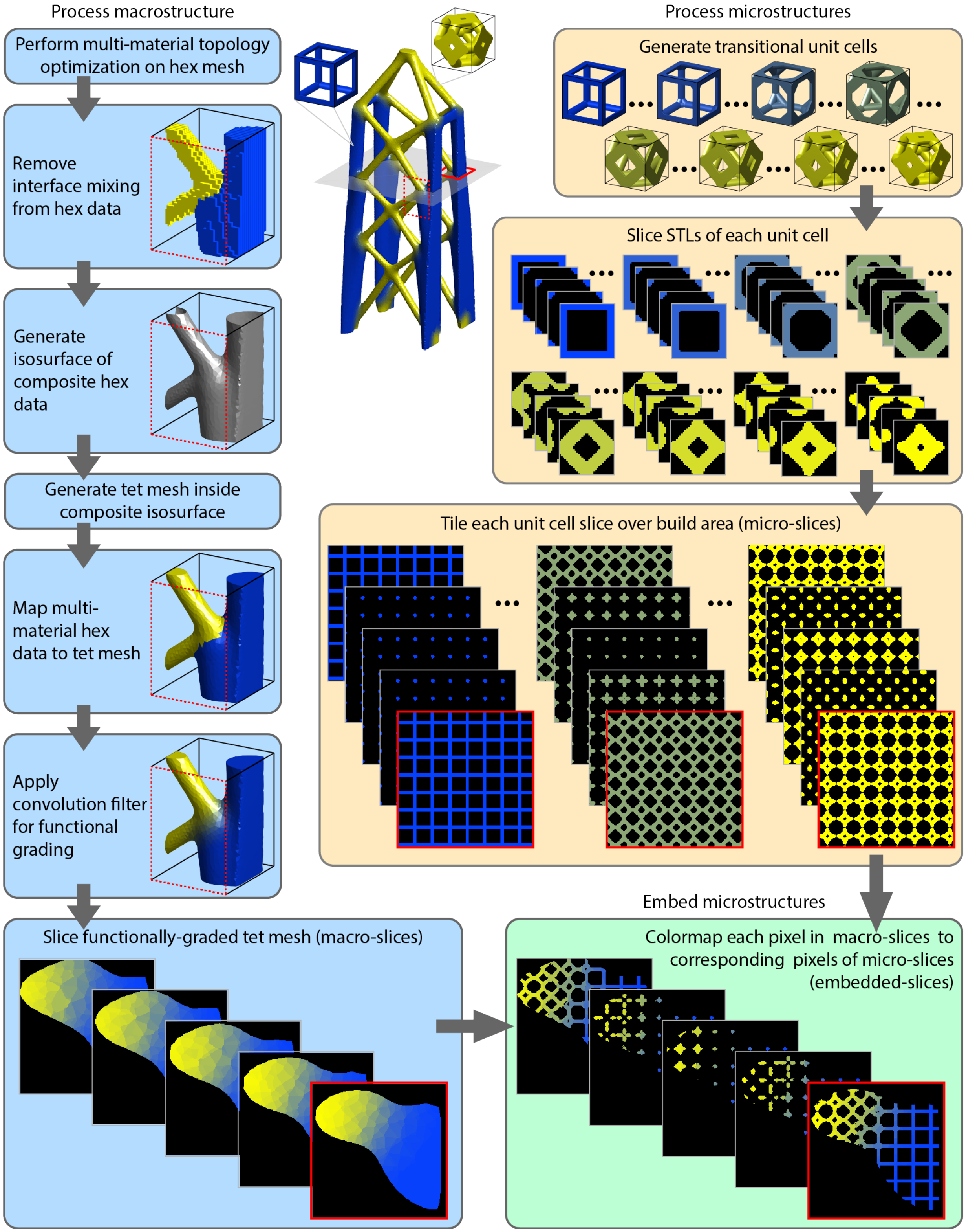

Fig. S3. Flowchart summarizing the overall process from design to manufacturing. On the left side, we perform multi-material topology optimization, process the multi-material density data, and slice the macrostructure. On the right side, we slice and tile the microstructures associated with the candidate microstructural-materials used in topology optimization. Finally, we embed the micro-slices into the macro-slices and send the embedded-slices to the 3D printer.

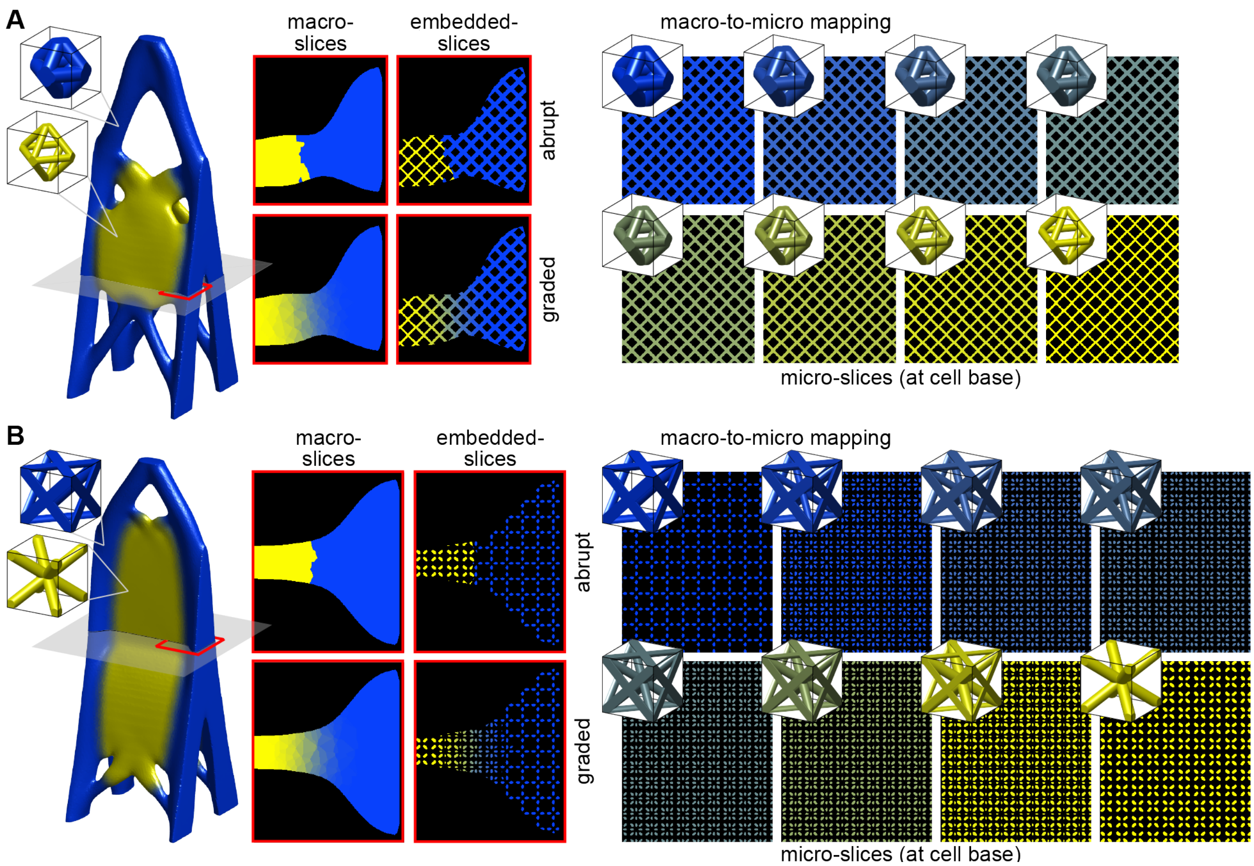

Fig. S4. Continuous multi-microstructure-embedding for two-microstructural-material cantilevers. The cantilevers are composed of (**A**) two octahedron unit cells with different bar diameter and (**B**) a face-x and a center-x unit cell. The transitional unit cells making up the macro-to-micro mapping in (**A**) are obtained by interpolating the bar diameter. Those in (**B**) are obtained by composing the two unit cells into a set of hybrid unit cells, where the face-x unit cell gradually disappears from one end and the center-x unit cell gradually disappears from the other (with minimum bar diameter limited to 0.065 of the unit cell edge length for manufacturability). In (**A**), 8 of the 14 transitional unit cells are shown and in (**B**), 8 of the 13 transitional unit cells are shown.

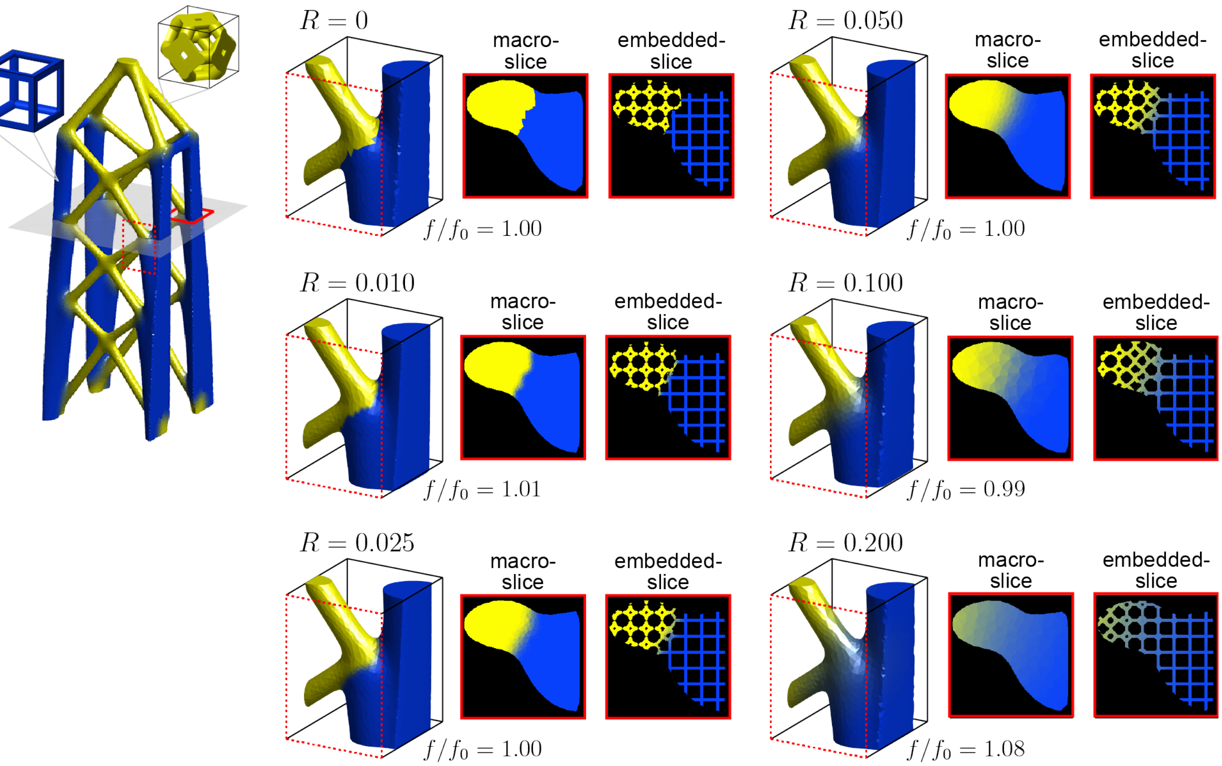

Fig. S5. Illustration of how the transition region length scale, microstructure connectivity, and objective function value are affected by the filter radius used in functional grading. The figure shows a closeup of a portion of the functionally-graded tet mesh and associated macro-slices and embedded-slices for $R = 0$ (abrupt interfaces), $R = 0.010$, $R = 0.025$, $R = 0.050$, $R = 0.100$, and $R = 0.200$. The objective function values, f/f_0, which are normalized to that of the case with R = 0, indicate that the length scale of the transition regions does not significantly affect the global elastic properties of the structure.

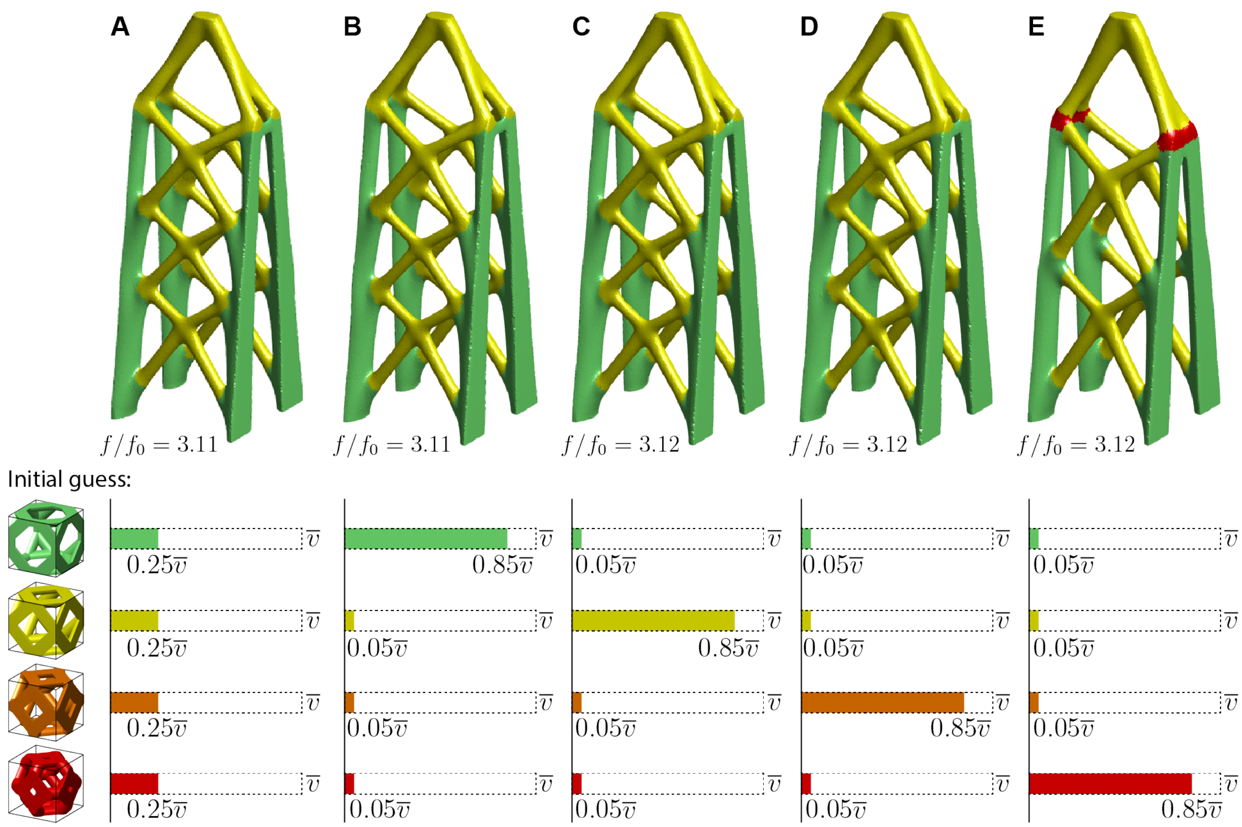

Fig. S6. Results considering different initial guesses for the example in Fig. 4F. (**A**) Uniform initial guess used in Fig. 4F. For each case in (**B** - **E**), one microstructural-material dominates the initial guess with its densities equal to $0.85\overline{v}$ and all other microstructural-material densities equal to $0.05\overline{v}$. The schematic at the bottom indicates the value of the design variables associated with each candidate material at the initial guess. Variable f_0 refers to the objective function value of the structure in Fig. 4A.

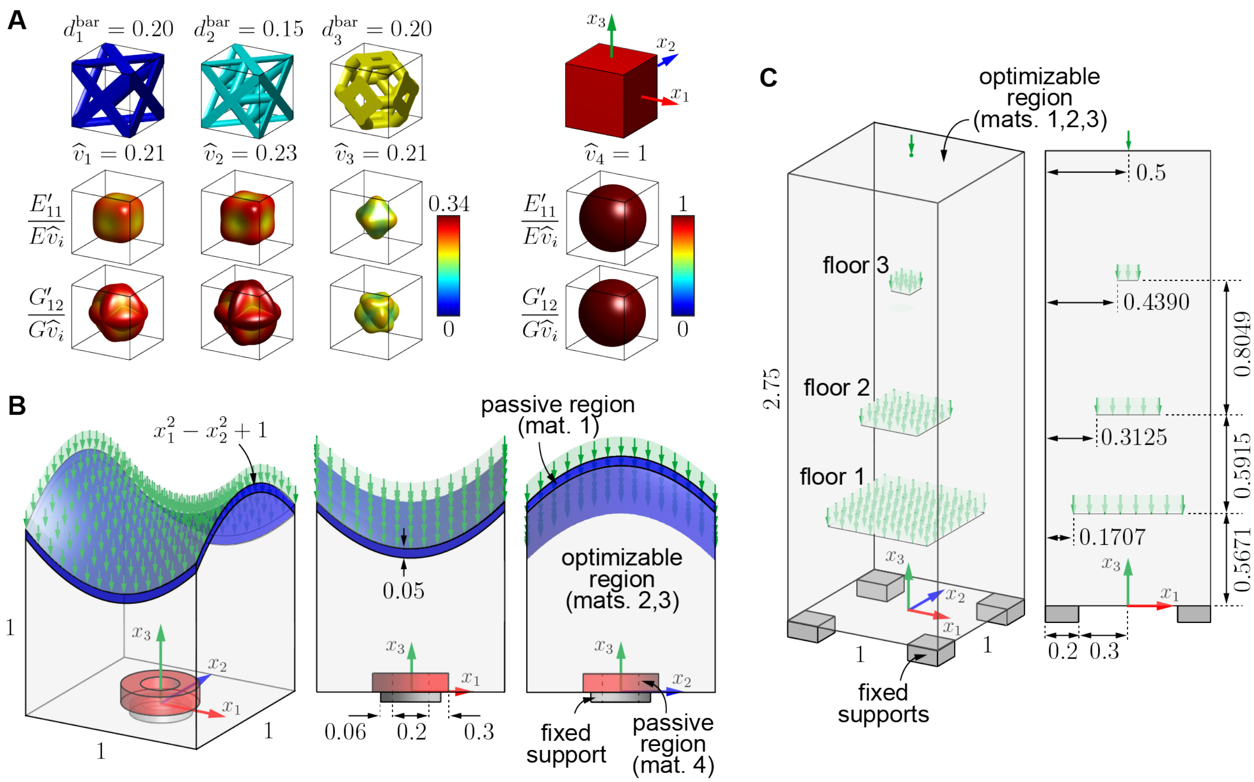

Fig. S7. Problem description for canopy and Eiffel Tower-inspired structures. (**A**) Candidate microstructural-materials and associated normalized, directional tensile and shear moduli plots. (**B**) Domain and boundary conditions for a hyperbolic paraboloid canopy structure subjected to a uniformly distributed, vertical load. The canopy is a passive region occupied by microstructural-material 1, the red tube near the base is a passive region occupied by solid, isotropic material 4, and the optimizable region can take microstructural-materials 2 and 3 with volume fraction limited to $\overline{v} = 0.0096$. (**C**) Domain and boundary conditions for an Eiffel Tower-inspired structure subjected to uniformly-distributed, vertical loads at each floor, where the total force for floors 1, 2, 3, and the top are 1, 0.766, 0.3, and 0.01, respectively. The optimizable region can take microstructural-materials 1, 2, and 3 with volume fraction of bulk material limited to $\overline{v} = 0.008$. The dimensions roughly mimic those of the Eiffel Tower (*49*).

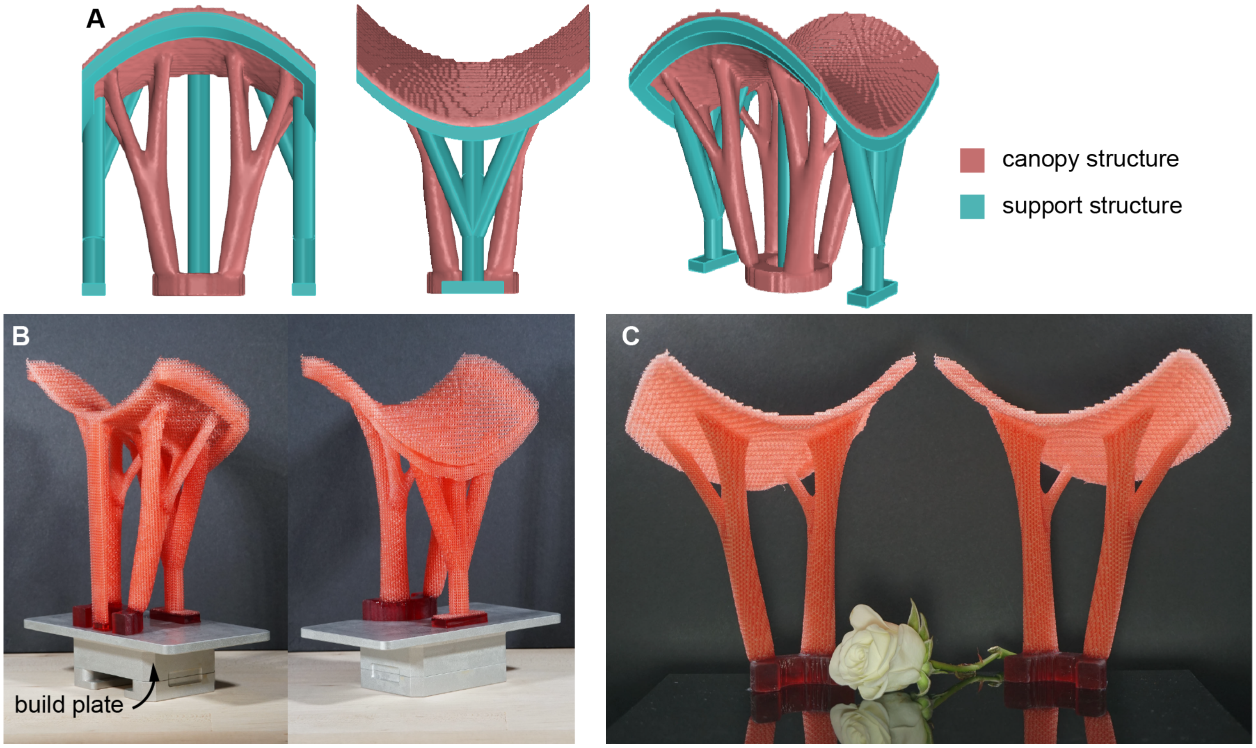

Fig. S8. Manufacturing details for canopy structure. (**A**) Support structures required for printing the canopy structure. (**B**) One half of the canopy structure before removing the support structure or removing it from the build plate. (**C**) Canopy structure after removing the support and before gluing the pieces together. Photo Credit: Emily D. Sanders, Georgia Institute of Technology.

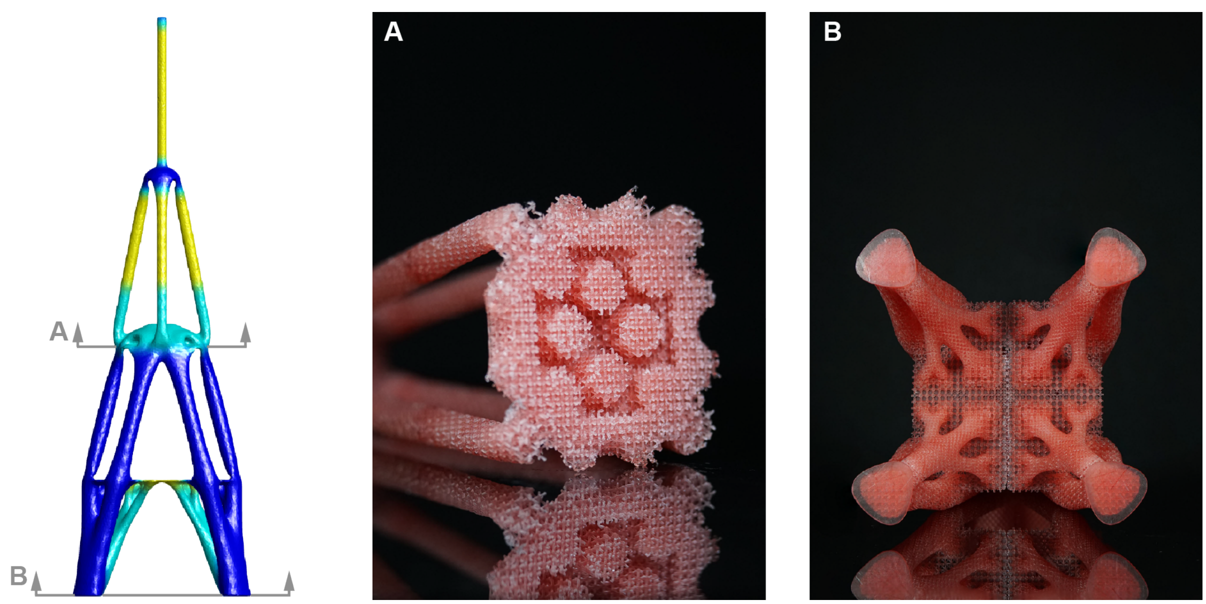

Fig. S9. Additional details of Eiffel Tower-inspired structure. (**A**) Cross-section through floor 2; (**B**) cross-section through base. Photo Credit: Emily D. Sanders, Georgia Institute of Technology.